Multifunctional nanomicelles constructed by aggregation and de-aggregation strategy for magnetic resonance/NIR II fluorescence imaging guided Type I photodynamic therapy

Lirong Wang[a,b#], Ji Qi[d#], Ke Zhang[e], Zeyan Zhuang[a,b], Keke Ding[f], Xu Chen[a,b], Hong Shan[e], Dan Ding[d], Anjun Qin[a,b,*], Ben Zhong Tang[b,c,g]

[a] *State Key Laboratory of Luminescent Materials and Devices, Guangdong Provincial Key Laboratory of Luminescence from Molecular Aggregates, South China University of Technology, Guangzhou 510640, China.*

[b] *Center for Aggregation-Induced Emission, AIE Institute, South China University of Technology, Guangzhou 510640, China.*

[c] *School of Science and Engineering, Shenzhen Institute of Aggregate Science and Engineering, The Chinese University of Hong Kong, Shenzhen, 518172, Guangdong, China.*

[d] *State Key Laboratory of Medicinal Chemical Biology, College of Life Sciences, Nankai University, Tianjin 300071, China.*

[e] *Center for Interventional Medicine, The Fifth Affiliated Hospital, Sun Yat-sen University, Zhuhai 519000, China.*

[f] *Department of Urology, The First Affiliated Hospital of Soochow University, Suzhou 215006, China.*

[g] *Hong Kong Branch of Chinese National Engineering Research Centre for Tissue Restoration and Reconstruction, The Hong Kong University of Science & Technology, Clear Water Bay, Kowloon, Hong Kong, China.*

* Corresponding author: E-mail:msqinaj@scut.edu.cn.

Abstract

Fluorescence and magnetic resonance imaging (FL/MRI) has received much attention from their complementary characteristics. However, the simultaneous enhancement of fluorescence and MR signals plus the efficacy of the treatment is still a major challenge. To solve this problem, we put forward a strategy of aggregation and de-aggregation based on aggregation-induced emission (AIE). NIR II photosensitizer TQ-TPA with Type I reactive oxygen species (ROS) generation ability and an amphiphilic 2TPE-Gd were firstly synthesized, and both of them showed the AIE property. Depending on the hydrophilic properties, hydrophobic TQ-TPA spontaneously aggregated into the core of nanomicelles formed by DSPE-PEG. Meanwhile, the aggregated 2TPE-Gd in aqueous solution could de-aggregate and insert in the interface, and formed TGdTT NMs. Based on this strategy and AIE property, TGdTT NMs exhibited strong NIR II fluorescence emission and Type I ROS generation ability, and enhanced T_1 relaxivity (r_1). Moreover, *in vitro*, *in vivo*, and pharmacokinetics results demonstrated these nanomicelles had good biosafety and long blood circulation time. Finally, they successfully realized complementary MR/NIR II fluorescence dual-modal imaging guided photodynamic therapy (PDT) to inhibit tumor growth. This work demonstrated that aggregation and de-aggregation strategy of AIEgens in the core-shell nanomicelle exudes infinite charm for constructing the multifunctional theranostic probes.

Keywords

1. **Introduction**

The combination of diagnostics and therapeutics, that is, theranostics, is a trend to fit clinical practice in fighting against cancer because it provides real-time feedback of treatment and holds great potential to enhance the accuracy of diagnosis and improve the efficacy of therapy, which afford superb therapeutic outcome. For the diagnostic system, multi-modal imaging guarantees the observation of the accurate tumor location at early stage [1-3], among which FLI/MRI is the most popular combination because of their complementary characteristics [4,5]. MRI owns the merit of high tissue penetration depth and spatial resolution but low sensitivity. This disadvantage just could be remedied by FLI. However, the penetration of light of fluorescence probes limits their further applications. Recently, NIR II organic fluorophores have received more and more attention because of their higher biosafety than inorganic ones, deeper penetration depth and higher signal to noise ratio than red or NIR FLI [6-10]. Therefore, how to integrate these fluorophores with MRI contrast agent (CA) to realize effective and multifunctional theranostic effect has been a hot and challenging field for researchers. In general, the conjugation of a fluorescent probe with a MRI CA, such as Magnevist® (Gd-DTPA) or Dotarem® (Gd-DOTA), could realize dual-modal FLI/MRI [11-14]. However, in most cases, the fluorescence intensity of conventional fluorophores can be easily quenched by the gadolinium complexes due to the heavy atom effect [11] or aggregation-caused quenching (ACQ) effect [15].

On the contrary, aggregation-induced emission luminogens (AIEgens) exhibit brighter emission in their aggregate states than in solutions because of the restriction of intramolecular motion (RIM), rendering them with tremendous advantages such as high fluorescence quantum yield, anti-photobleaching effect, and long-term tracing for *in vivo* imaging [16,17]. In addition, some AIEgens bearing strong electron donor (D) and acceptor (A) could serve as photosensitizers (PSs) to simultaneously enhance fluorescence and ROS generation ability [18,19]. Among the AIE PSs, the ones that mostly generate Type I ROS (H_2O_2, $O_2^{•-}$, $•OH$, etc.), have attracted tremendous attentions owing to the stronger hypoxia tolerance than traditional PSs that mainly generate Type II ROS ($^1O_2$) [20-23], which are the excellent alternative material for PDT [24]. Therefore, conjugating AIEgens with GBCA to form AIE-Gd probes would be an ideal candidate to construct dual-modal imaging and therapeutic agents. Because the aggregation of AIEgens could not only enhance the fluorescence intensity but also the large size of AIE-Gd aggregates could prolong the rotational correlation time (τ_R) [25,26] to improve the r_1. However, AIE-Gd aggregates generally show enhanced emission upon aggregation in aqueous solution due to the amphipathic property, but their r_1 usually improves slightly [27]. This could be attributed to the tight aggregation of AIE-Gd hindering the accessibility of Gd to water molecules in the bulk solution although they have larger size than non-aggregation, thus leading to the low efficiency in improving r_1. These results suggested that simply aggregating AIE-Gd amphipathic molecules is not an effective strategy for

enhancing their MRI performance. How to control their aggregation in a loose structure for the diffusion of water molecules, which could increase the accessibility to slowly diffusing water molecules of Gd [28-30], would be a strategy to simultaneously enhance the fluorescence intensity and r_1.

Tetraphenylethylene (TPE) is a typical AIE molecule, which has been usually utilized to design new AIEgens. In 2011, Tang's group reported that the aggregates of amphiphilic TPE derivatives could be easily de-aggregated by the incorporation of enough surfactant, resulting in the weakened emission [31]. This de-aggregation could form micelles with TPE derivatives interspersing in the shell of micelles. As is known to us, nanomicelles (NMs) is a good nano-delivery system, which has received widespread attention in biomedical field because of their facile preparation, large loading capacity, and good biocompatibility, making them highly translatable for biomedical applications [32]. Moreover, the interior and interface of NMs could load different functional molecules according to their hydrophilicity and hydrophobicity for theranostics [33,34]. This inspired us to utilize the surfactant to load different multifunctional AIEgens. Based on the differences in hydrophilicity, they would be dispersed in the core and shell of micelles respectively through aggregation and de-aggregation process. Herein, we firstly synthesized a hydrophobic molecule 4,4'-(6,7-diphenyl-[1,2,5]thiadiazolo[3,4-g]quinoxaline-4,9-diyl) bis(*N*,*N*-diphenylaniline) (TQ-TPA) and an amphipathic molecule 2TPE-Gd-DOTA (2TPE-Gd), both of them showed AIE property. Then, 1,2-distearoyl-sn-glycerol-3-phosphoethanolamine-*N*-methoxy (polyethylene glycol)-2000 (DSPE-PEG) was chosen to load these two molecules with the feeding weight ratio of 16:16:1 (TQ-TPA:DSPE-PEG:2TPE-Gd) to form NMs (named as TGdTT NMs), which realized the improvement of r_1 by keeping these two molecules dispersed in the interface and core of the NMs respectively (Fig. 1). As expected, these multifunctional TGdTT NMs have a spherical morphology with the size of 52.2 ± 10.2 nm, exhibiting NIR absorbing, NIR II emission, and high Type I ROS generation ability. Meanwhile, the r_1 of TGdTT NMs showed a 5-fold increase compared with those of clinical MRI CA of Gd-DOTA. Accordingly, TGdTT NMs with good biocompatibility and biosafety realized the MR/NIR II FL dual-modal imaging both *in vitro* and *in vivo* and effective Type I ROS for cancer cell killing and tumor inhibition. All these results confirmed that our designed TGdTT NMs would be a fabulous Type I PS for MR/NIR II FL imaging guided PDT.
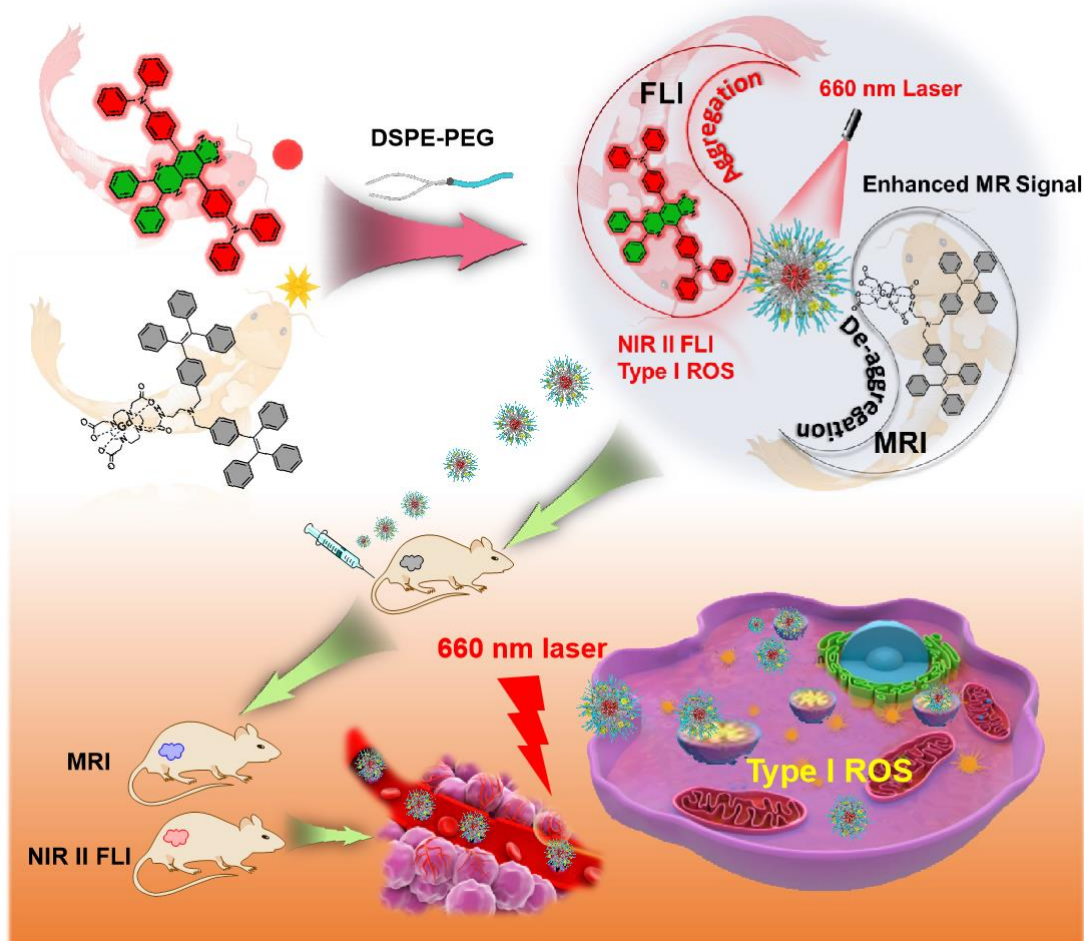
Fig. 1. Schematic illustration of the construction of TGdTT NMs and their application in MR/NIR II FL dual-mode imaging guided Type I photodynamic therapy.

2. Experimental section

2.1. Materials

All chemicals, unless otherwise noted, were purchased from commercial sources and used without further purification. $GdCl_3$ was purchased from Alfa Aesar. 1,4,7,10-Tetra-azacyclododecane (min. 98% CYCLEN) was purchased from Strem Chemicals Inc. Bromotriphenylethylene and 4-bromo-*N*,*N*-diphenylaniline were obtained from Soochiral Chemical Science & Technology Co., Ltd. *N*-Bromosuccinimide was purchased from J&K Scientific LTD. 4-Tolylboronic acid were obtained from Alfa Aesar. Azobisisobutyronitrile (AIBN), potassium carbonate (K_2CO_3) and magnesium sulfate ($MgSO_4$) were purchased from Aladdin Co., Ltd. Tetrakis(triphenylphosphine)palladium ($Pd(PPh_3)_4$) were obtained from Energy Co., Ltd. Ultra-filtration units (Amicon Ultra 15 mL Filters with 30 kDa nominal molecular weight cutoff) were purchased from Merck Millipore Corp.

2.2. Synthesis of *N*,*N*-diphenyl-4-(tributylstannyl)aniline (2)

4-Bromo-*N*,*N*-diphenylaniline (**1**, 4.86 g, 15 mmol) was added into a 250 mL of Schlenk flask. The flask was then vacuumed and purged with dry nitrogen three times, and anhydrous THF (80 mL) was added. Then the mixture was cooled to -78 °C, and maintained at this temperature for 15 min, followed by the addition of *n*-butyllithium (*n*BuLi, 2.5 M hexane solution, 6 mL, 15 mmol). After stirring at this temperature for 2 h, tri-*n*-butyltin chloride (4.6 mL, 17 mmol) was added, and the mixture was slowly warmed to room temperature, and stirred overnight. Then water was added to quench the reaction, and the mixture was extracted with DCM for three times. The organic phase was combined and dried over anhydrous $MgSO_4$. After removal of the solvent under reduced pressure, the crude product (**2**) was used for the next reaction without further purification. ^{1}H NMR (400 MHz, $CDCl_3$, 25 °C) δ (ppm): 7.31 (t, 2H), 7.24 (t, 4H), 7.09 (d, 4H), 7.05-6.97 (m, 4H), 1.60-1.51 (m, 6H), 1.36-1.27 (m, 6H), 1.12-1.09 (m, 6H), 0.98 (t, 9H).

2.3. Synthesis of 4,4'-(5,6-dinitrobenzo[*c*][1,2,5]thiadiazole-4,7-diyl)bis(*N*,*N*-diphenylaniline) (4)

N,*N*-diphenyl-4-(tributylstannyl)aniline (**2**, 6.4 g, 12 mmol), 4,7-dibromo-5,6-dinitrobenzo[*c*][1,2,5]thiadiazole (**3**, 1.92 g, 5 mmol), and Pd(PPh₃)₄ (335 mg, 0.3 mmol) were added into a 250 mL of two-necked round-bottom flask. The flask was then vacuumed and purged with dry nitrogen three times, and anhydrous THF (150 mL) was added. The mixture was refluxed for 24 h. After cooling down to room temperature, water was added to quench the reaction, and the mixture was washed with DCM three times. The organic phase was combined, dried over $MgSO_4$, and the solvent was evaporated under reduced pressure. The crude product was purified by silica gel column chromatography using dichloromethane/hexane (1:2 v/v) as the eluent. A dark purple solid (**4**) was obtained in 72% yield (2.56 g). ^{1}H NMR (400 MHz, $CDCl_3$): δ 7.41(d, 4H), 7.33 (t, 8H), 7.22 (d, 8H), 7.13 (t, 8H).

2.4. Synthesis of 4,7-bis(4-(diphenylamino)phenyl)benzo[*c*][1,2,5]thiadiazole-5,6-diamine (5)

To the mixture of compound **7** (1.43 g, 2 mmol) and acetic acid (150 mL) in a 250 mL of two-necked round-bottom flask, iron powder (3.36 g, 60 mmol) was added. The mixture was heated to 80 °C, and stirred for 6 h. After cooling down to room temperature, water was added, and the mixture was washed with DCM three times. The organic phase was combined, dried over $MgSO_4$, and the solvent was evaporated under reduced pressure. The crude product (**5**) was used directly for the next step without further purification.

2.5. Synthesis of 4,4'-(6,7-diphenyl-[1,2,5]thiadiazolo[3,4-*g*]quinoxaline-4,9-diyl)bis(*N*,*N*-diphenylaniline) (TPA-TQ)

Compound **5** (196 mg, 0.3 mmol) and benzil (**6**, 126 mg, 0.6 mmol) were dissolved in the mixture of chloroform (20 mL) and acetic acid (20 mL) in a 100 mL flask. The reaction mixture was heated to 60 °C, and stirred for 12 h. Then water was added, and the mixture was extracted with DCM three times. The organic phase was combined, and dried over anhydrous MgSO$_4$. After the removal of the solvent under reduced pressure, the residue was purified by silica gel column chromatography using DCM/hexane (1:2 v/v) as the eluent. A dark blue solid of **TPA-TQ** was obtained in 72% yield (178.7 mg,). ^{1}H NMR (400 MHz, CDCl$_3$, 25 °C) δ (ppm): 7.98 (d, 4H), 7.66 (d, 4H), 7.38 (d, 2H), 7.37-7.25 (m, 24H), 7.10 (t, 4H). ^{13}C NMR (100 MHz, CDCl$_3$, 25 °C) δ (ppm): 153.13, 152.73, 148.04, 147.55, 138.58, 136.06, 134.02, 130.08, 129.56, 129.35, 128.57, 128.22, 128.19, 125.18, 123.39, 121.61, 99.99. HRMS (MALDI-TOF) calculated for C$_{56}$H$_{39}$N$_6$S [M+H]$^+$ m/z: 827.2957, found: 827.2954.

2.6. Synthesis of tri-tert-butyl 2,2',2''-(10-(2-((2-(bis(4-(1,2,2-triphenylvinyl)benzyl)amino)ethyl)amino)-2-oxoethyl)-1,4,7,10-tetraazacyclododecane-1,4,7-triyl)triacetate (9)

Tri-tert-butyl-2,2',2''-(10-(2-((2-aminoethyl)amino)-2-oxoethyl)-1,4,7,10-ertraazacyclododecane-1,4,7-triyl)triacetate (DOTAtBu-NH$_2$) (**7**,100 mg, 0.16 mmol) was synthesized according to previous reports [35]. It was dissolved in acetonitrile, followed by addition of K$_2$CO$_3$ (27.6 mg, 0.2 mmol). Compound **8** (135.6 mg, 0.32 mmol) dissolved in acetonitrile was added dropwise into the above solution. After finishing the addition, the solution was refluxed for 1 h. After filtration and solvent evaporation, the crude product was purified by silica gel column chromatography using dichloromethane/methanol (10:1 v/v) as the eluent. A white powder (**9**) was obtained in 98% yield (207.9 mg). ^{1}H NMR (400 MHz, CDCl$_3$): δ 7.37 (s, 1H), 7.15-6.82 (m, 38H), 5.27 (s, 1H), 3.56 (d, 32H), 1.43 (d, 27H).^{13}C NMR (100 MHz, CDCl$_3$): δ 172.55, 171.03, 143.26, 141.85, 140.72, 137.44, 131.59, 128.34, 127.16, 126.09, 81.82, 57.24, 56.36, 55.71, 53.56, 52.90, 28.04. HRMS (MALDI-TOF) calculated for C$_{84}$H$_{98}$N$_6$O$_7$Na [M+Na]$^+$ m/z: 1325.7385, found: 1325.7395.

2.7. Synthesis of compound 2TPE-Gd

Compound **9** (100 mg, 0.08 mmol) was dissolved in 5 mL trifluoroacetate acid (TFA) at room temperature. After stirring for 6 h, excess TFA was removed by rotary evaporation. And then, the resultant white solid product was dissolved in methanol, and the pH of the solution was adjusted to 5~6 with dilute sodium hydroxide solution. Afterward, anhydrous gadolinium chloride (24 mg, 0.09 mmol) in 3 mL methanol was added dropwise into the solution. After reaction overnight at 60 °C, methanol was removed by evaporation. The crude product was re-dissolved in DCM, and the excess gadolinium ions were washed away with water. A white solid of **2TPE-Gd** was obtained

in 90% yield (92.9 mg). HRMS (MALDI-TOF) calculated for $C_{72}H_{72}N_6O_7Gd$ $[M+H]^+$ m/z: 1290.4703; found: 1290.4673.

2.8. Cell Culture

Murine breast cancer 4T1 cells were cultured in Dulbecco's modified eagle medium (DMEM) containing 10% fetal bovine serum at 37 $^{\circ}C$ in a humidified environment containing 5% CO_2.

2.8.1. Cell colocation by Confocal Microscopy

4T1 cells were seeded at a density of 2×10^4 cells per plate on a 35 mm dish. Cells were incubated with the Gd(III) concentration (10 μM) of TGdTT NMs for 4 h, and then washed twice with PBS. Fresh media with lysotracker red (2 μM) was added and further incubated for 15 min. Then cells were washed three times with PBS and fresh media was added for confocal fluorescence imaging using a Zeiss LSM 710 confocal laser scanning. The excitation wavelength of 405 nm and emission of 410-520 nm were set for TGdTT NMs, while those for Lysotracker red were 570 nm and 590-700 nm, respectively.

2.8.2. Cell Viability without Laser Irradiation

The cytotoxicity of TGdTT NMs were assessed by the 3-(4, 5-dimethylthiazol-2-y1)-2, 5-diphenyltetrazolium bromide (MTT) assay. 4T1 cells were firstly seeded into a 96-well plate at a density of 5000 cells/well in DMEM and incubated for 24 h. Then the media was replaced with TGdTT NMs at different Gd(III) concentrations (0, 1.56, 3.13, 6.25, 12.5, 25, 50 μM) and cells were incubated for additional 24 h. After incubation, the culture media were removed and each well was filled with 100 μL of fresh culture media containing MTT (0.5 mg/mL) and incubation for additional 4 h. Then the media was discarded and each well was added with another 100 μL DMSO. The OD490 value (Abs.) of each well was measured by microplate reader immediately. Cell viability was expressed by the ratio of OD490 values of the cells incubated with TGdTT NMs suspension to that of the cells incubated with culture medium only.

2.8.3. *In vitro* MR imaging and Cell uptake

4T1 cells at a density of 1×10^7/dish were seeded into three tissue culture dishes respectively. After incubation for 24 h, these media were replaced by the media with TGdTT NMs and Gd-DOTA both at the same Gd(III) concentration (30 μM) or PBS. The cells were washed with PBS for three times and harvested into 200 μL microcentrifuge tube. T_1-weighted phantom images of cells were obtained on a 0.5 T NMR120-Analyst system with parameters: TR = 100 ms and TE = 5.3 ms. The intensities at regions of interest (ROI) were quantified by ImageJ. After imaging tests, the Gd contents of these samples were analyzed by ICP-MS.

2.9. *In vivo* MRI

Animal experiments were executed according to the protocol approved by Institutional Animal Care and Use Committee (IACUC) of South China University of Technology. Clinical CA Gd-DOTA was used as a control. MR imaging was conducted on a 9.4 T MRI scanner. The same slices were acquired at different time (0, 1, 4, 7, and 24 h) after intravenous injection. All the images were obtained using T1_ FLASH sequence with parameters as follows: TR/TE = 300/3.0 ms. MR contrast-to-noise ratio (CNR) was evaluated by finely analyzing ROIs of tumor and surrounding tissue. CNR = $|SNR_{tumor}-SNR_{tissue}|/SNR_{tissue}$. And contrast enhancement was defined as CNR_{post}/CNR_{pre}.

2.10. *In vivo* FLI

Female BALB/c mice bearing subcutaneous 4T1 tumors were intravenously injected with TGdTT NMs at the dose of 0.5 g/kg body weight. Fluorescence images were collected at indicated time (0, 1, 4, 7, and 24 h) using Full Spectrum Animal *In Vivo* Imaging System AniView Phoenix 600 (Guangzhou Biolight Biotechnology Co., Ltd).

2.11. Pharmacokinetics

To determine the blood circulation half-lives, TGdTT NMs were intravenously injected into healthy female BALB/c mice ($n = 3$/group) at the dose of 0.5 g/kg body weight. At predestinated time (10 min, 20 min, 0.5 h, 1 h, 2 h, 4 h, 8 h, 12 h, and 24 h) after injection, approximate 20 μL blood was collected from the tail. The amount of Gd(III) in these samples were measured by ICP-MS. The final amount of Gd(III) were calculated as the percentage of the injected dose per gram tissue (% ID/g).

2.12. Biodistribution

4T1 tumor-bearing female BALB/c mice were injected with TGdTT NMs at a dose of 0.5 g/kg body weight, and were sacrificed at 4, 7, and 24 h post injection ($n = 3$/group), respectively. Heart, liver, spleen, lung, kidney, intestine, and tumors were collected and weighed. The amount of Gd(III) in these samples were measured using ICP-MS. The final amount of Gd(III) was calculated as the percentage of the injected dose per gram tissue (% ID/g).

2.13. *In vivo* efficacy

The subcutaneous tumor was constructed by injecting 1×10^6 4T1 cells at the right hind leg of female BALB/c mouse. After the volume of tumor was about 50 mm^3, these tumor-bearing mice were randomly divided into four groups ($n = 3$/group): PBS group, only TGdTT NMs, only laser, TGdTT NMs plus laser irradiation group. In order to obtain effective tumor inhibition, the

treatment of injection and laser irradiation was carried out every four days. The tumor volume and body weight were measured every other day. The tumor volume was calculated according to the equation: tumor volume = (tumor length) × (tumor width)^2/2. Relative tumor volumes were calculated as V/V_0 (V is the tumor volume before treatment).

2.14. Biosafety assessment

The healthy female BALB/c mice (n = 3/group) were intravenously injected with TGdTT NMs at a dose of 0.5 g/kg body weight. PBS was served as a control. After 30 days, blood samples were collected from the orbital sinus by quickly removing the eyeball from the socket with a pair of tissue forceps. Then, liver function index including alanine aminotransferase (ALT), aspartate aminotransferase (AST), albumin (ALB) and renal function index including creatinine (Cr), uric acid (UA), urea (UREA) were detected. In addition, the tissues of mice (heart, liver, spleen, lung, kidney) were collected to be sectioned and stained with hematoxylin and eosin for histological assessment.

2.15. Statistical analysis

Least-significant difference (LSD) tests were used to determine whether the variance between groups is similar. The sample size (n = 3) was chosen to evaluate the statistical analysis, which was performed using SPSS (IBM Corp.). Statistical significance was calculated using two-tailed LSD tests and defined as *$P < 0.001$.

3. Results and Discussion

3.1. Synthesis and Characterization of TQ-TPA and 2TPE-Gd

To obtain low-bandgap AIE PS, the D-π-A strategy was generally employed. In this work, we chose thiadiazolo[3,4-g]quinoxaline (TQ) and triphenylamine (TPA) as the accepting and donating moieties to build the targeted molecule TQ-TPA, and its synthetic route is shown in Fig. 2A. The intermediates and target molecule were characterized by ^{1}H and ^{13}C NMR spectra (Fig. S1-S4). Afterwards, the photophysical property of TQ-TPA was investigated. As expected, TQ-TPA shows an absorption peak at 630 nm and broad emission spectrum with peak at 917 nm and tail to 1200 nm (Fig. 2B). Moreover, the photoluminescent (PL) spectra of TQ-TPA in THF/water mixture showed that when the water fraction (f_w) values were lower than 60%, its emission gradually weakened due to the twisted intramolecular charge transfer (TICT) process, afterward, the emission intensified because of the formation of aggregates and activation of RIM process (Fig. S5).

For ROS generation ability of TQ-TPA, we used 2',7'-dichlorofluorescein (DCFH) as total ROS indicator to explore. To make it better disperse in water, TQ-TPA was fabricated into nanomicelles by encapsulation with DSPE-PEG at the weight ratio of 1:1. As shown in Fig. 2C and Fig. S6, the fluorescence intensity of DCFH incubated with 20 µM of TQ-TPA NMs exhibited a 500-fold improvement compared with that of only DCFH under 660 nm laser irradiation at the power of 0.3 W/cm^2. Furthermore, TQ-TPA NMs also showed a concentration-dependent ROS generation ability. Even at a low concentration of 5 µM, TQ-TPA NMs exhibited a 280-fold enhancement compared with that of only DCFH under the same conditions. Next, we used Type I indicator of hydroxyphenyl fluorescein (HPF) and Type II indicator of 9,10-anthracenediyl-bis(methylene)-dimalonic acid (ABDA) to identify the types of ROS. The remarkable increased PL intensity of HPF suggested that TQ-TPA mainly generated hydroxyl radicals (•OH, Type I ROS) (Fig. 2D). Meanwhile, the slightly decreased absorption intensity of ABDA (Fig. 2E and Fig. S7) suggested that the singlet oxygen ($^1O_2$, Type II ROS) was hardly generated.

To have a detail insight into the favorable generation of Type I ROS of TQ-TPA, we carried out theoretical study using M06-2X/6-311G(d,p) and M06-2X/def2-TZVP program in Gaussian 16. The results indicated the highest occupied molecular orbital (HOMO) and lowest unoccupied molecular orbital (LUMO) of optimized TQ-TPA structure at ground state (S_0) and excited states (S_1 and T_1) are separated and distributed in TPA and TQ moiety respectively (Fig. S8A). Meanwhile, the spin-orbit coupling (SOC, 0.65 cm^{-1}) was high enough to elicit a more efficient intersystem crossing process. Moreover, the energy gap between T_1 and S_0 is only 0.21 eV, which is inadequate to provide the energy required for oxygen to be excited to $^1O_2$ species (0.95 eV). While, the TQ-TPA$^•$ in the T_1 state could easily obtain electron from adjacent substance to produce TQ-TPA$^{•-}$, from which the electron could transfer to the surrounding tissue to eventually generate •OH species (Fig. S8B). Therefore, all of the above results indicated that we have obtained the NIR II emitted Type I AIE PSs.

3.2. Synthesis and Characterization of 2TPE-Gd

Meanwhile, we combined TPE with Gd complex to explore their interaction with DSPE-PEG. As shown in Scheme S1, the methylbromide group connected to TPE was allowed to react with tri-tert-butyl-2,2',2''-(10-(2-((2-aminoethyl)amino)-2-oxoethyl)-1,4,7,10-ertraazacyclododecane-1,4,7-triyl)triacetate (DOTAtBu-NH$_2$) at a molar ratio of 2:1. After deprotection of the ester groups by trifluoroacetic acid, gadolinium irons were chelated to product the probe of 2TPE-Gd, which were structurally confirmed by NMR spectral characterization (Fig. S9 and Fig. S10). Its absorption (Fig. S11A) and emission peaks in THF (Fig. S11B) were recorded at 320 and 470 nm, respectively. The PL spectra measurement in THF/water mixture with different f_w indicated that 2TPE-Gd is also AIE active (Fig. S11B and Fig. S11C). In addition, 2TPE-Gd had a low critical micelle concentration (CMC) of 4.9 µM (Fig. S12A and Fig. S12B), suggesting that it could easily

form micelles in aqueous solution. These properties facilitated it to interact with DSPE-PEG for exploring the effect on relaxivity. In water, 2TPE-Gd gave strong blue emission because of the formation of aggregates. However, its PL intensity gradually decreased upon addition of DSPE-PEG due to de-aggregation of the molecules (Fig. 2F), and the trade-off value was recorded as the weight ratio of DSPE-PEG/2TPE-Gd of 16:1 (Fig. 2G and Fig. S13). Interestingly, the relaxation rate gradually increased with increasing of DSPE-PEG and also reached the maximum at the weight ratio of 16:1 (Fig. 2H). The reason might be that with the increase of DSPE-PEG, the 2TPE-Gd aggregates were de-aggregated by DSPE-PEG to gradually form lager size of micelles, which could prolong the τ_R of these micelles. Meanwhile, PEGs could hold enough water molecules to lengthen the diffusion correlation time (τ_D) of these water molecules, which ensured the exchange rate of gadolinium with water protons [28]. All these factors contributed to the improvement of r_1. Furthermore, with the increase of DSPE-PEG, the encapsulation efficiency of 2TPE-Gd also enhanced to be more than 85% finally (Fig. S14). Therefore we used this ratio in the construction of micelles.
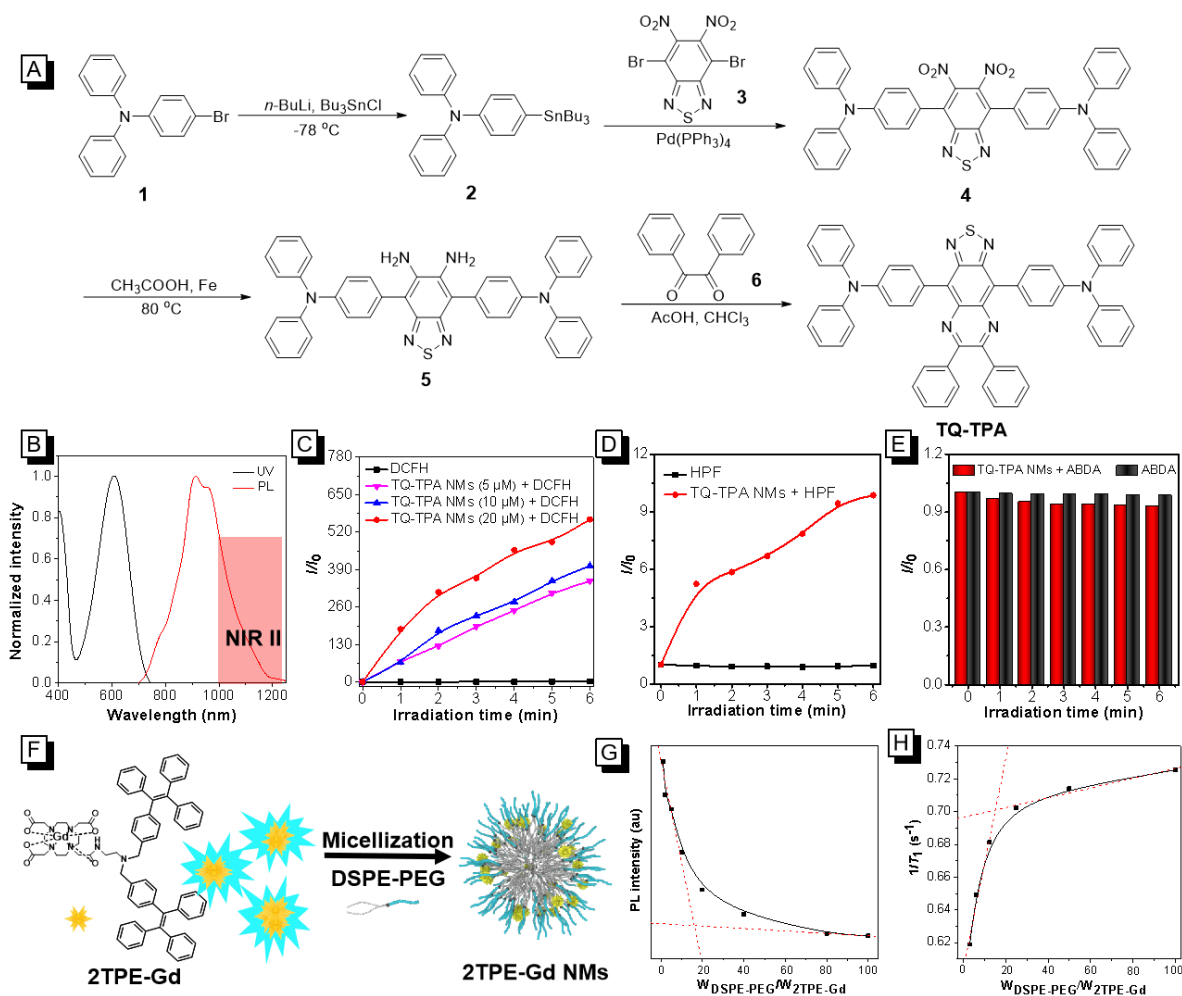
Fig. 2. The synthesis and property characterization of TQ-TPA and 2TPE-Gd. (A) The synthetic route of TQ-TPA. (B) The absorption and PL spectra of TQ-TPA in THF solution (10 μM). (C) ROS generation of different concentrations (5, 10, and 20 μM) of TQ-TPA NMs under 660 nm laser irradiation (0.3 W/cm^2) using DCFH as an indicator. (D) Plots of relative PL intensity of HPF (for •OH detection) with or without TQ-TPA NMs under 660 nm laser irradiation (0.3 W/cm^2). (E) The decomposition rates of ABDA (100 μM) with or without TQ-TPA NMs under 660 nm laser irradiation (0.3 W/cm^2). (F) Schematic illustration of aggregation of 2TPE-Gd with strong fluorescence in water and de-aggregation of 2TPE-Gd by the insertion of DSPE-PEG to form 2TPE-Gd nanomicelles, leading to the decrease in fluorescence intensity. (G) PL intensity of 2TPE-Gd (10 μM) upon addition of different weight of DSPE-PEG. The inset is the fluorescence images at different weight ratio of DSPE-PEG/2TPE-Gd. (H) The relaxation rate of different weight ratio of DSPE-PEG/2TPE-Gd with the certain concentration (50 μM) of 2TPE-Gd.

3.3. Construction and Characterization of TGdTT NMs

After successfully obtained AIE Type I PS and amphiphilic AIE-Gd, we constructed TGdTT NMs by self-assembly of TQ-TPA/DSPE-PEG/2TPE-Gd with the feeding weight ratio of 16:16:1 (Fig. 3A). The transmission electron microscopy (TEM) measurement showed that TGdTT NMs had a spherical morphology with the size of 52.2 ± 10.2 nm, which was consistent with the result of dynamic light scattering (DLS) of 91.3 ± 3.9 nm (Fig. 3B). Notably, TGdTT NMs could be stable in phosphate buffer solution (PBS) for more than 15 days (Fig. S15). The absorption and PL spectra of TGdTT NMs were similar with those of TQ-TPA NMs (Fig. 3C). Moreover, the PL quantum yield of TGdTT NMs (~3%, Fig. S16A) was almost same as that of TQ-TPA NMs (Fig. S16B), indicating that the introduction of 2TPE-Gd had no interference on the emission property of TQ-TPA. Subsequently, we compared the ROS generation ability of TGdTT NMs, TQ-TPA NMs, and Ce6. The results showed that fluorescence intensity of DCF in TGdTT NMs aqueous solution was slightly lower than that in TQ-TPA NMs aqueous solution, but was still much higher than that of Ce6 at the same experimental conditions (Fig. S17). This might be attributed that gadolinium complex quenched the emission of DCF indicator in some extent due to the ACQ property of DCF molecules.

We next evaluated the r_1 values of TGdTT NMs, 2TPE-Gd NMs, 2TPE-Gd, and clinical MRI CA Gd-DOTA at a 0.5 T MRI scanner. As shown in Fig. 3D and listed in Table S1, the relaxivity of TGdTT NMs was recorded to be 32.5 ± 0.6 mM^{-1}s^{-1}, which was not only higher than that of 2TPE-Gd NMs (25.3 ± 0.8 mM^{-1}s^{-1}), but also 3- and 6-time larger than those of 2TPE-Gd (10.5 ± 0.6 mM^{-1}s^{-1}) and Gd-DOTA (5.2 ± 0.2 mM^{-1}s^{-1}). The reason might be that the larger size of nanomicelles attenuate the rotation of 2TPE-Gd and diffusion of water molecules trapped in the DSPE-PEG chains compared with 2TPE-Gd and Gd-DOTA, which could be identified by the hydration diameters of TGdTT NMs (91.3 ± 3.9 nm), 2TPE-Gd NMs (78.8 ± 5.4 nm), 2TPE-Gd

(5.6 ± 0.4 nm), and Gd-DOTA (0.8 ± 0.03 nm), respectively (Fig. 3E and Table S1). Thus, all of above results indicated that TGdTT NMs would be a very attractive platform integrating of NIR II emission, high MR contrast, and efficient Type I ROS generation ability for biological applications.
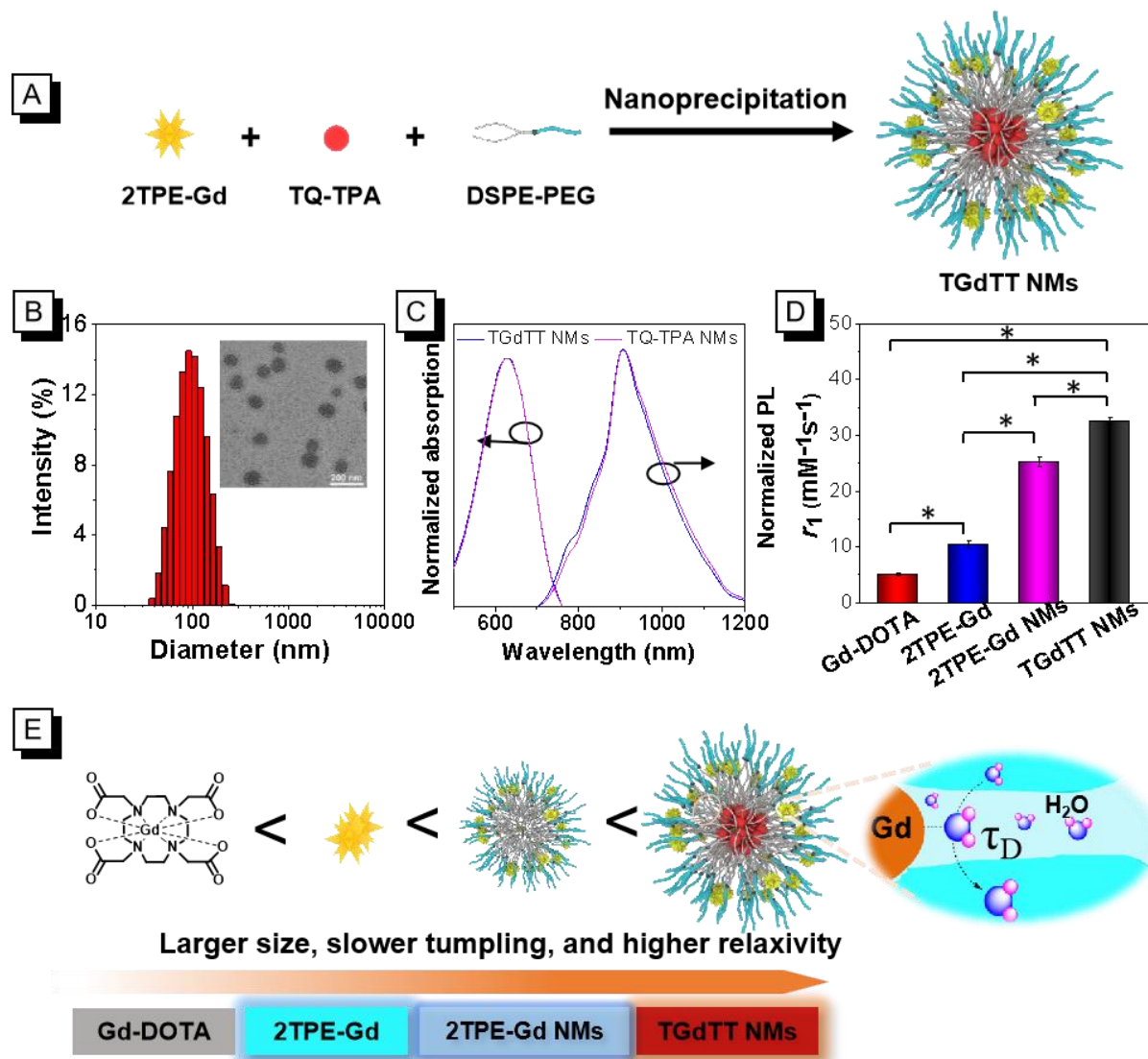

Fig. 3. Construction and characterization of TGdTT NMs. (A) Construction procedure of TGdTT NMs. (B) DLS results of TGdTT NMs. The insert is the TEM of TGdTT NMs. (C) Normalized absorption and PL spectra of TGdTT NMs and TQ-TPA NMs in aqueous solution. (D) Relaxivities of TGdTT NMs, 2TPE-Gd NMs, 2TPE-Gd, and Gd-DOTA at 0.5 T (n = 3). Data are reported as mean ± SD and analyzed using one-way ANOVA and followed by LSD's test. *P < 0.001. (E) Illustration of the mechanism of enhancement of relaxivity from 2TPE-Gd to TGdTT NMs.

3.4. Bimodal NIR II FL/MRI *in vitro* and cell killing of TGdTT NMs

Subsequently, we explored their applications in cancer cells imaging and killing. First, the biocompatibility of TGdTT NMs was evaluated by tetrazolium-based colorimetric assays, and the result suggested that TGdTT NMs had good biocompatibility even at high Gd(III) concentration of 50 μM (Fig. S18). The confocal laser scanning microscope (CLSM) measurement revealed that TGdTT NMs could light up cells, and mainly located in lysosome, which was confirmed by cell co-localization experiment (Fig. 4A and Fig. S19). Furthermore, the T_1-weighted phantom images in *in vitro* experimental results demonstrated that TGdTT NMs showed higher contrast signal than that of Gd-DOTA at 0.5 T (Fig. 4B and Fig. 4C). Notably, inductively coupled plasma mass (ICP-MS) spectroscopy test showed that the amount of TGdTT NMs and Gd-DOTA uptake by cells was 117.78 ± 2.98 and 118.22 ± 5.24 fg Gd(III)/cell. These results demonstrated that TGdTT NMs had better T_1-weighted contrast ability than Gd-DOTA at same Gd(III) concentration *in vitro*.

To evaluate the ROS generation ability of TGdTT NMs in cell level, 2′,7′-dichlorodihydrofluorescein diacetate (DCFH-DA) was chosen as indicator, which could easier permeate the cell membrane than hydrolyzed DCFH and be deacetylated to DCFH by intracellular esterase to detect ROS. As shown in Fig. S20, the 4T1 cancer cells showed bright green emission in the TGdTT NMs group under laser irradiation. While, there was no emission observed in the cells with sole TGdTT NMs, only laser irradiation or in PBS group (Blank). Because of the superb Type I ROS generation ability, the cells viability obviously decreased with increasing concentration of TGdTT NMs at 660 nm laser irradiation for 5 min (Fig. 4D). The calcein AM/propidium iodide experiments suggested that TGdTT NMs with photo-irradiation demonstrated efficient cancer cell killing ability (Fig. 4E).
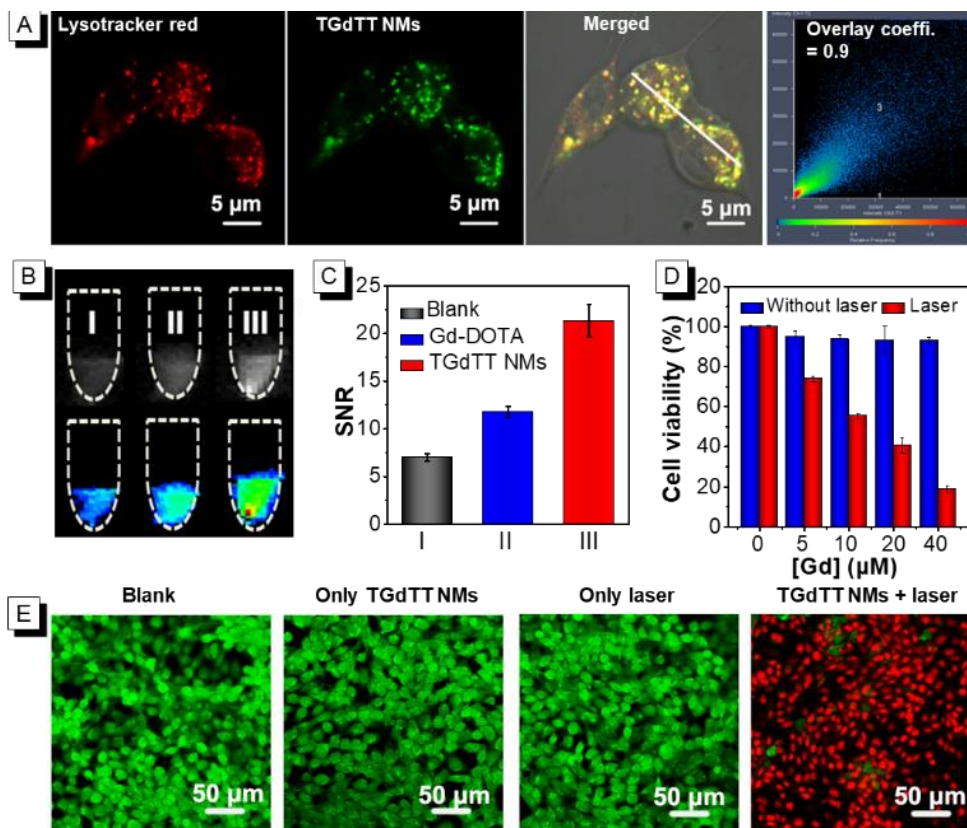
Fig. 4. Cell imaging and *in vitro* PDT. (A) Colocalization imaging of TGdTT NMs and lysotracker red by CLSM. (B) 4T1 cell phantom images of blank (I), Gd-DOTA (II), and TGdTT NMs (III) at 0.5 T. (C) The signal-to-noise ratio (SNR) of phantom images in (B). (D) Cell viability of TGdTT NMs by MTT with or without 660 nm laser irradiation (0.3 W/cm^2, 5 min). (E) Dead and live 4T1 cells co-staining assays using propidium iodide (Red, Dead cell) and Calcein-AM (Green, live cell) as fluorescence probes.

3.5. Bimodal MR/NIR II FLI of TGdTT NMs *in vivo* and pharmacokinetic evaluation

Besides cell level, TGdTT NMs were also applied in subcutaneous 4T1 tumor bearing mice to show their dual-modal imaging and therapy. Based on the excellent T_1-weighted contrast ability of TGdTT NMs, we first explored the MRI of tumor-bearing female Balb/c mice at 9.4 T MRI scanner, and clinical MRI CA Gd-DOTA was used as a control. After intravenous injection of TGdTT NMs, T_1-weighted MR images were collected at different times. As shown in Fig. 5A, remarkable T_1-weighted contrast signals were observed in the tumor region, and the signal strength of tumor reached to maximum at 7 h post-injection. In comparison, due to the low r_1 and rapid renal clearance, weak contrast signals could be observed in Gd-DOTA group with the same dose of Gd(III), which was also confirmed by relative contrast-to-noise ratio (CNR$_{post}$/CNR$_{pre}$) [15,36]. At 7 h post-injection, the CNR$_{post}$/CNR$_{pre}$ of TGdTT NMs group was 12 times higher than that of Gd-DOTA group (Fig. 5B), demonstrative of excellent imaging performance of TGdTT NMs.

These results confirmed that TGdTT NMs could enhance T_1-weighted tumor contrast and permit long-term MRI imaging of tumor.

Taking advantages of deep penetration depth and high signal-to-noise ratio of NIR II FLI, we subsequently used the NIR II FLI of TGdTT NMs to validate their accumulation at tumor sites. As shown in Fig. 5C, the emission peak was observed at 7 h post-injection, and the fluorescence signal has become weak at 24 h post-injection. This result was consistent with that of T_1-weighted MRI. Based on the high tissue penetration depth and spatial resolution of MRI and excellent sensitivity and signal-to-noise ratio of FLI, the tumor site and geometry could be delineated comprehensively, being beneficial for tumor therapy. These results unambiguously demonstrated that TGdTT NMs are excellent MRI/NIR II FLI dual-modal probes for tumor imaging, which could precisely locate tumor sites and further guide PDT.

To further evaluate the uptake of TGdTT NMs by tumors *in vivo*, blood circulation and bio-distribution of TGdTT NMs were studied by measuring Gd(III) concentrations in the blood and tissues at different time. The blood circulation curve showed that there was a steady-state period from 0.5 to 4 h (Fig. 5D), which provided TGdTT NMs with enough time to circulate in the body and accumulate in the tumor through enhanced permeability and retention (EPR) effect [37]. The bio-distribution study suggested that they mainly accumulated in liver, spleen, intestine, and tumor (Fig. 5E). This result suggests that they were mainly withheld in liver and spleen by reticuloendothelial system and excreted through hepatobiliary route [38,39].
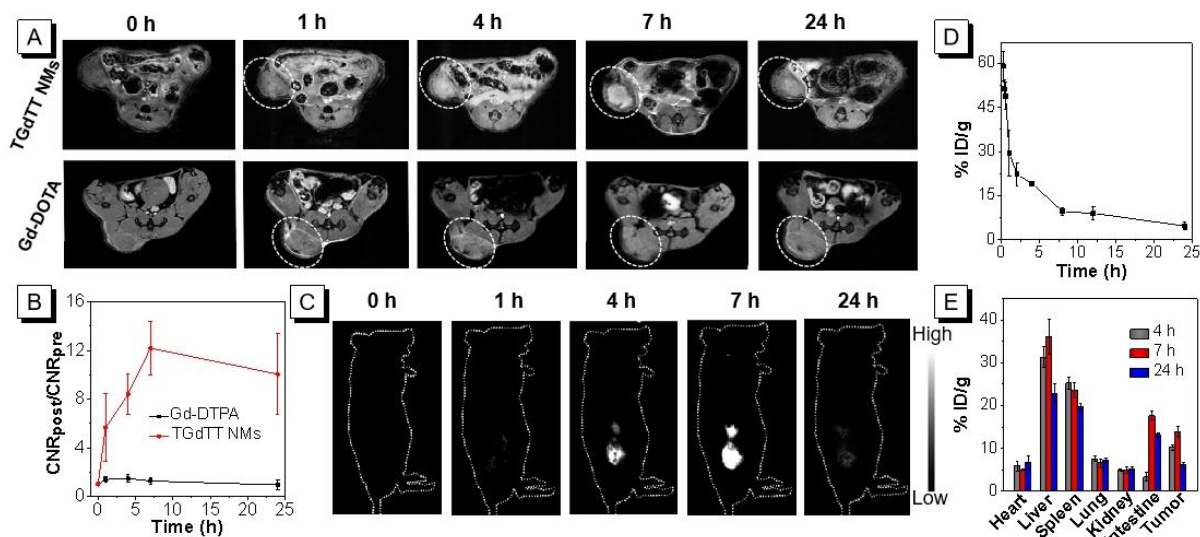

Fig. 5. Dual-modal *in vivo* MRI/NIR II FLI. (A) MRI of 4T1 tumor-bearing mice at 0, 1, 4, 7, and 24 h after intravenous injection of TGdTT NMs (0.5 g TGdTT NMs/kg body weight). (B) CNR_{post}/CNR_{pre} of tumor signals of MRI at different time. (C) NIR II FLI of 4T1 tumor-bearing mice at 0, 1, 4, 7, and 24 h after intravenous injection of TGdTT NMs (0.5 g TGdTT NMs/kg body weight). (D) Blood circulation curves of TGdTT NMs in the blood at different time after

intravenous injection (n = 3). (E) Tissue distribution of TGdTT NMs in 4T1 tumor-bearing mice at 0, 4, 7, and 24 h after intravenous injection (n = 3/group).

3.6. PDT for tumor inhibition and biosafety evaluation

Under the guidance of dual-modal MR/NIR II FL imaging, the ablation ability of subcutaneous tumor by 660 nm light induced PDT was explored. After intravenous injection of TGdTT NMs for 7 h, the 4T1 tumor-bearing female mice were irradiated for 10 min. During the treatment, the injection and laser irradiation were carried out every four days as shown in Fig. 6A, and the tumor volume and body weight were detected every two days. After treatment for three times, the experiments of tumor sections stained by hematoxylin and eosin (H&E) showed that TGdTT NMs with laser irradiation group had sparse nucleus compared with dense cancer cell nucleus of control groups of sole TGdTT NMs, only laser, or PBS (Fig. 6B), indicating that most of cancer cells had been killed. In addition, the relative tumor volume of control groups obviously increased by 8~12 times. In sharp contrast, the tumor growth in TGdTT NMs with laser irradiation group was greatly inhibited (Fig. 6C and Fig. S21). These results verified that TGdTT NMs could generate enough Type I ROS upon photo-irradiation to inhibit the tumor growth. Notably, during treatment period, the mice weights in the four groups showed similar growth trend (Fig. 6D), suggesting that there was no detectable side effect of these treatments for mice.

To evaluate the biosafety of TGdTT NMs, they were intravenously injected into healthy female BALB/c mice, and PBS was used as the control. After 30 days, these mice were sacrificed and their blood and major tissues were collected to evaluate the biosafety. The H&E staining of major organs revealed that histologically no cell necrosis or inflammation occurred (Fig. S22). In addition, the indices of liver and renal function tests also showed no noticeable abnormalities (Fig. S23). All of these results demonstrated that TGdTT NMs show excellent biocompatibility for theranostic applications.
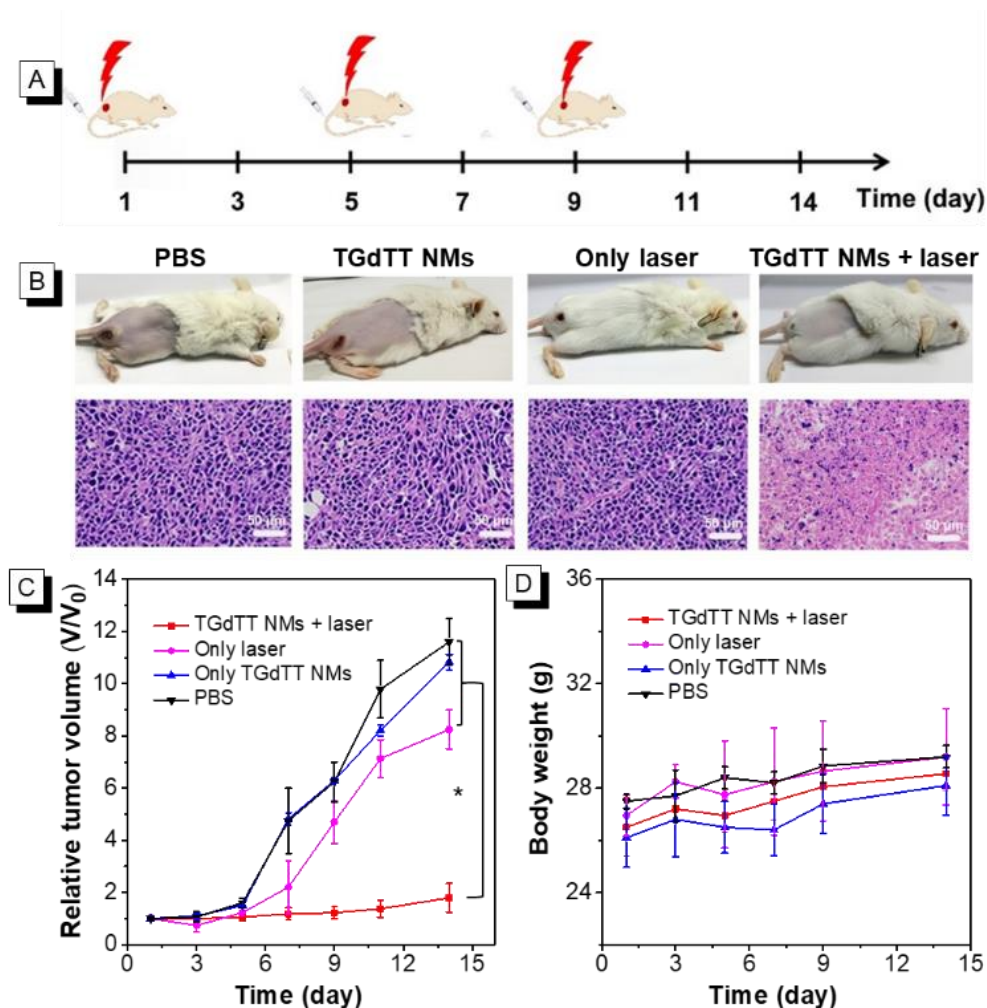
Fig. 6. *In vivo* efficacy of TGdTT-mediated PDT. (A) *In vivo* treatment timeline. (B) Representative digital photographs and H&E staining tumor slices of mice treated with PBS, sole TGdTT NMs, only laser, and TGdTT NMs with laser irradiation after treatment. (C and D) Tumor growth curves and body weight changes of mice after various treatments (n = 3/group). Error bars indicate standard deviations of means. *P < 0.001.

4. Conclusion

In this work, a novel strategy based on the aggregation and de-aggregation of two AIEgens for the construction of TGdTT NMs with dual-modal MRI/NIR II FLI and PDT effect was presented. TGdTT NMs were composed with the aggregation of hydrophobic TQ-TPA in their core and de-aggregation of amphipathic 2TPE-Gd in the interface of DSPE-PEG nanomicelles. Notably, the r_1 of Gd(III) complexes in TGdTT NMs increased significantly because of the attenuation of the rotation of 2TPE-Gd with the large size of NMs and water diffusion trapped in the DSPE-PEG chains. Moreover, excellent NIR II emission and Type I ROS generation have also been achieved for TGdTT NMs owing to the containing TQ-TPA molecules. Because of their enhanced r_1, high

ROS generation ability, excellent biocompatibility and biosafety, as well as relatively long blood circulation time to passively target to the tumor, TGdTT NMs realized the dual-modal MRI/NIR II FLI guided PDT, which greatly inhibited the tumor growth. We believe this work provides a new strategy for researchers to construct multifunctional nanomaterials based on AIE for improved theranostic applications.

Data Availability

Data will be made available on request.

CrediT authorship contribution statement

Lirong Wang: Conceptualization, Methodology, Formal analysis, Investigation, Visualization, Writing – original draft, Project administration. **Ji Qi:** Investigation. **Ke zhang:** Investigation. **Hong Shan:** Investigation. **Zeyan Zhuang:** Investigation. **Keke Ding:** Investigation. **Xu Chen:** Investigation. **Dan Ding:** Investigation. **Anjun Qin：** Conceptualization, Project administration, Resources, Supervision, Writing – review & editing, Funding acquisition. **Ben Zhong Tang:** Project administration, Resources, Supervision, Funding acquisition. #These authors contributed equally.

Appendix A. Supporting information

Supplementary data associated with this article can be found in the online version.

References

[1] D.E. Lee, H. Koo, I.C. Sun, J.H. Ryu, K. Kim, I.C. Kwon, Chem. Soc. Rev. 41 (2012) 2656-2672.

[2] D.S. Karaman, M.P. Sarparanta, J.M. Rosenholm, A.J. Airaksinen, Adv. Mater. 30 (2018) e1703651.

[3] B. Qiao, Y. Luo, H.B. Cheng, J. Ren, J. Cao, C. Yang, B. Liang, A. Yang, X. Yuan, J. Li, L. Deng, P. Li, H.T. Ran, L. Hao, Z. Zhou, M. Li, Y. Zhang, P.S. Timashev, X.J. Liang, Z. Wang, ACS Nano 14 (2020) 12652-12667.

[4] V.S. Talanov, C.A. Regino, H. Kobayashi, M. Bernardo, P.L. Choyke, M.W. Brechbiel, Nano Lett. 6 (2006) 1459-1463.

[5] P. Verwilst, S. Park, B. Yoon, J.S. Kim, Chem. Soc. Rev.44 (2015) 1791-1806.

[6] Q. Yang, Z. Ma, H. Wang, B. Zhou, S. Zhu, Y. Zhong, J. Wang, H. Wan, A. Antaris, R. Ma, X. Zhang, J. Yang, X. Zhang, H. Sun, W. Liu, Y. Liang, H. Dai, Adv. Mater. 29 (2017) 1605497.

[7] S. Zhu, Q. Yang, A.L. Antaris, J. Yue, Z. Ma, H. Wang, W. Huang, H. Wan, J. Wang, S. Diao, B. Zhang, X. Li, Y. Zhong, K. Yu, G. Hong, J. Luo, Y. Liang, H. Dai, Proc. Natl. Acad. Sci. U S A 114 (2017) 962-967.

[8] L. Lu, B. Li, S. Ding, Y. Fan, S. Wang, C. Sun, M. Zhao, C.X. Zhao, F. Zhang, Nat. Commun. 11 (2020) 4192.

[9] J. Qi, N. Alifu, A. Zebibula, P. Wei, J.W.Y. Lam, H.-Q. Peng, R.T.K. Kwok, J. Qian, B.Z. Tang, Nano Today 34 (2020) 100893.

[10] Z. Ma, F. Wang, W. Wang, Y. Zhong, H. Dai, Proc. Natl. Acad. Sci. U S A 118 (2021).

[11] M.H. Lee, E.J. Kim, H. Lee, H.M. Kim, M.J. Chang, S.Y. Park, K.S. Hong, J.S. Kim, J.L. Sessler, J. Am. Chem. Soc. 138 (2016) 16380-16387.

[12] H. Li, G. Parigi, C. Luchinat, T.J. Meade, J. Am. Chem. Soc. 141 (2019) 6224-6233.

[13] R. Yan, Y. Hu, F. Liu, S. Wei, D. Fang, A.J. Shuhendler, H. Liu, H.Y. Chen, D. Ye, J. Am. Chem. Soc. 141 (2019) 10331-10341.

[14] H. Li, D. Luo, C. Yuan, X. Wang, J. Wang, J.P. Basilion, T.J. Meade, J. Am. Chem. Soc. 143 (2021) 17097-17108.

[15] V.S. Harrison, C.E. Carney, K.W. MacRenaris, E.A. Waters, T.J. Meade, J. Am. Chem. Soc. 137 (2015) 9108-9116.

[16] H. Li, H. Kim, J. Han, V.N. Nguyen, X. Peng, J. Yoon, Aggregate 2 (2021) e51.

[17] Y.L. Balachandran, X. Jiang, CCS Chemistry 4 (2022) 420-436.

[18] F. Hu, S. Xu, B. Liu, Adv. Mater. 30 (2018) e1801350.

[19] T. Zhou, R. Hu, L. Wang, Y. Qiu, G. Zhang, Q. Deng, H. Zhang, P. Yin, B. Situ, C. Zhan, A. Qin, B.Z. Tang, Angew. Chem. Int. Ed. 59 (2020) 9952-9956.

[20] Z. Zhuang, J. Dai, M. Yu, J. Li, P. Shen, R. Hu, X. Lou, Z. Zhao, B.Z. Tang, Chem. Sci. 11 (2020) 3405-3417.

[21] D. Chen, Q. Xu, W. Wang, J. Shao, W. Huang, X. Dong, Small 17 (2021) e2006742.

[22] M. Kang, Z. Zhang, W. Xu, H. Wen, W. Zhu, Q. Wu, H. Wu, J. Gong, Z. Wang, D. Wang, B.Z. Tang, Adv. Sci. (Weinh) 8 (2021) e2100524.

[23] Q. Sun, Q. Su, Y. Gao, K. Zhou, W. Song, P. Quan, X. Yang, Z. Ge, Y. Zhang, G. He, Aggregate (2022).

[24] T.C. Pham, V.-N. Nguyen, Y. Choi, S. Lee, J. Yoon, Chem. Rev. 121 (2021) 13454-13619.

[25] J. Hu, S. Liu, Sci. China Chem. 61 (2018) 1110-1122.

[26] J. Wahsner, E.M. Gale, A. Rodriguez-Rodriguez, P. Caravan, Chem. Rev. 119 (2019) 957-1057.

[27] Y. Chen, M. Li, Y. Hong, J.W. Lam, Q. Zheng, B.Z. Tang, ACS Appl. Mater. Interfaces 6 (2014) 10783-10791.

[28] J.S. Ananta, B. Godin, R. Sethi, L. Moriggi, X. Liu, R.E. Serda, R. Krishnamurthy, R. Muthupillai, R.D. Bolskar, L. Helm, M. Ferrari, L.J. Wilson, P. Decuzzi, Nat. Nanotechnol. 5 (2010) 815-821.

[29] A.G. Robertson, L.M. Rendina, Chem. Soc. Rev. 50 (2021) 4231-4244.

[30] L. Wang, Q. Wan, R. Zhang, B. Situ, K. Ni, J. Gao, X. Feng, P. Zhang, Z. Wang, A. Qin, B.Z. Tang, ACS Nano 15 (2021) 9924-9934.

[31] C. Zhu, S. Pang, J. Xu, L. Jia, F. Xu, J. Mei, A. Qin, J. Sun, J. Ji, B. Tang, Analyst 136 (2011) 3343-3348.

[32] A. Bose, D. Roy Burman, B. Sikdar, P. Patra, IET Nanobiotechnol. 15 (2021) 19-27.

[33] H. Gong, Z. Dong, Y. Liu, S. Yin, L. Cheng, W. Xi, J. Xiang, K. Liu, Y. Li, Z. Liu, Adv. Funct. Mater. 24 (2014) 6492-6502.

[34] H. Cao, Y. Yang, J. Li, Aggregate 1 (2020) 69-79.

[35] L. Wang, H. Lin, X. Chi, C. Sun, J. Huang, X. Tang, H. Chen, X. Luo, Z. Yin, J. Gao, Small 14 (2018) e1801612.

[36] J. Zhang, N. Chen, H. Wang, W. Gu, K. Liu, P. Ai, C. Yan, L. Ye, J. Colloid. Interface Sci. 469 (2016) 86-92.

[37] A. Nel, E. Ruoslahti, H. Meng, ACS Nano 11 (2017) 9567-9569.

[38] K. Yang, J. Wan, S. Zhang, Y. Zhang, S.T. Lee, Z. Liu, ACS Nano 5 (2011) 516-522.

[39] N. Sharma, M.A. Saifi, S.B. Singh, C. Godugu, In vivo studies: toxicity and biodistribution of nanocarriers in organisms, Nanotoxicity 2020, pp. 41-70.